CHEMISTRY OF MATERIALS

pubs.acs.org/cm

Article

Magnetic Ordering and Structural Transition in the Ordered Double-Perovskite Pb_2NiMoO_6

Jianfa Zhao, Xiao Wang, Xi Shen, Christoph J. Sahle, Cheng Dong, Hajime Hojo, Yuki Sakai, Jun Zhang, Wenmin Li, Lei Duan, Ting-Shan Chan, Chien-Te Chen, Johannes Falke, Cheng-En Liu, Chang-Yang Kuo, Zheng Deng, Xiancheng Wang, Richeng Yu, Runze Yu,* Zhiwei Hu,* Martha Greenblatt, and Changqing Jin*

Cite This: *Chem. Mater.* 2022, 34, 97−106

Read Online

ACCESS | Metrics & More | Article Recommendations | Supporting Information

ABSTRACT: The B-site-ordered double-perovskite Pb_2NiMoO_6 was prepared at high pressure and high temperature. The structural analysis of synchrotron powder X-ray diffraction data shows that Pb_2NiMoO_6 crystallizes into monoclinic symmetry with the space group *Pc* (no. 7), where the Ni and Mo ions are ordered in a rock-salt-type manner. The magnetic and specific heat characterizations reveal unusual two-step antiferromagnetic (AFM) transitions at 18 and 26 K for Pb_2NiMoO_6. The X-ray absorption spectra at the Ni-$L_{2,3}$ edge and the Mo-L_3 edge and the high-resolution partial fluorescence yield at the Pb-L_3 edge indicate $Pb^{2+}{}_2Ni^{2+}Mo^{6+}O_6$ valence states. Although in A_2NiMoO_6 (A = Sr^{2+}, Pb^{2+}, and Ba^{2+}), the size of the A cation increases gradually from Sr^{2+} (1.44 Å) to Pb^{2+} (1.49 Å) to Ba^{2+} (1.61 Å), Pb_2NiMoO_6 exhibits much lower symmetry structure and AFM transition temperature, T_N, compared with Sr_2NiMoO_6 (*I*4/*m*, T_N = 81 K) and Ba_2NiMoO_6 (*Fm*$\bar{3}$*m*, T_N = 64 K), which is attributed to the large distortion of NiO_6 and MoO_6 octahedra induced by the lone pair electron effect of Pb^{2+} with a $6s^2$ electronic configuration. Moreover, symmetry-breaking phase transition from a high-temperature centrosymmetric, cubic *Fm*$\bar{3}$*m* phase to a low-temperature non-centrosymmetric, monoclinic *Pc* phase was observed at 393−413 K in Pb_2NiMoO_6.

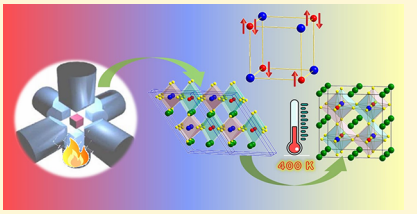

INTRODUCTION

ABO_3 perovskite-type oxides and derivatives present rich physical properties, owing to the cross interplay and correlation of lattice, charge, spin, and orbital degrees of freedom.[1−7] In ABO_3 perovskites, the A-site is usually occupied by alkaline, alkaline-earth, or lanthanide cations with 12-coordinated oxygen atoms, while the B-site often is accommodated by transition-metal ions with 6-coordinated oxygens.[8] The large radius of A-site ions generally stabilizes the three-dimensional perovskite crystal structure, while the transition metals in the B-site dominate the transport and magnetic properties of compounds.[9] Substitution of cation B′ for B leads in general to the solid solution $AB_{1-x}B'_xO_3$; however, if x = 0.5 and B and B′ differ sufficiently in charge and/or size, then the B-site cation ordering may occur.[10] The formula is then properly written as $A_2BB'O_6$, and the compound is described as a double perovskite. The common orderings that occur in such compounds are rock-salt, columnar, or layered ordering of B and B′ cations over the parent B sites.[11] The ideal structure of $A_2BB'O_6$-type B-site-ordered double perovskite can be viewed as a regular alternating arrangement of corner-sharing BO_6 and $B'O_6$ octahedra with no distortion.[12] Thus, these compounds usually crystallize into *Fm*$\bar{3}$*m* space group.[13] However, when the A-site cation is relatively small, a mismatch between the equilibrium (A−O) and (B−O)/(B′−O) bond lengths occurs, and the BO_6 and $B'O_6$ octahedra will distort accompanied by a decrease in the symmetry from cubic to tetragonal or even to monoclinic.[14] For example, in the double-perovskite family of A_2FeOsO_6 (A = Ca, $Ca_{0.5}Sr_{0.5}$, and Sr), the crystal symmetry is reduced from tetragonal *I*4/*m* (A = Sr) to monoclinic $P2_1/n$ (A = $Ca_{0.5}Sr_{0.5}$ and Ca) with decreasing A-site size.[13] High-pressure synthesis is a powerful technique to stabilize $A_2BB'O_6$-type B-site-ordered double perovskites with various sizes of ions. The pronounced effects of pressure are to shorten atomic bond distances, to enhance charge transfer, and to initiate chemical reactions thermodynamically forbidden at ambient pressure.[15,16] Thus, at high pressure, many new materials in general and new phases with $A_2BB'O_6$-type B-site-ordered double-perovskite structures in particular, which cannot form at ambient pressure, become stable/metastable.[17−19]

Compared to the simple ABO_3 perovskite, both B and B′-sites can accommodate transition-metal ions in $A_2BB'O_6$

Received: August 16, 2021
Revised: December 3, 2021
Published: December 21, 2021

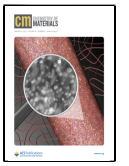

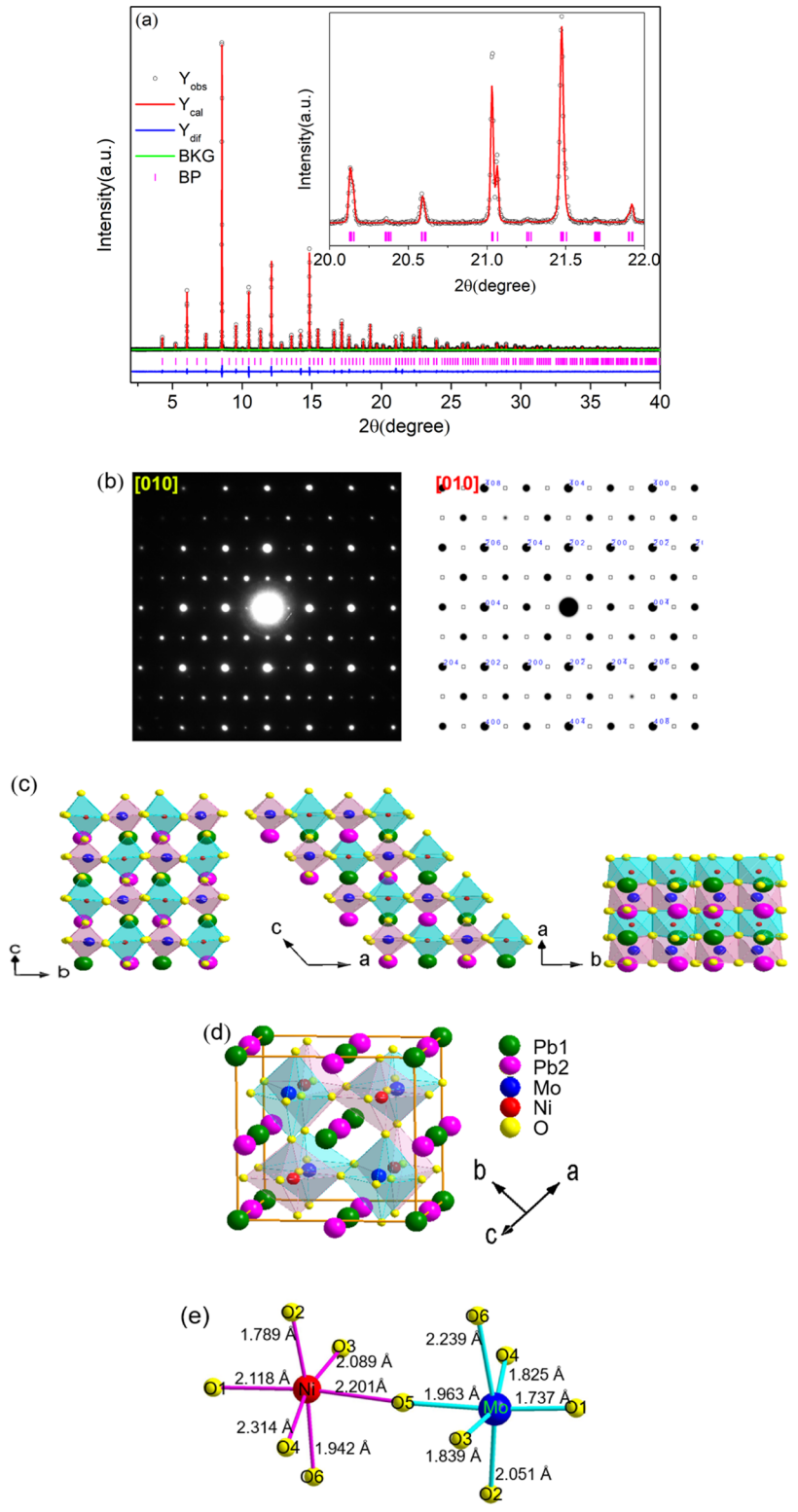

Figure 1. (a) Rietveld structural refinement results for PNMO of SXRD data collected at room temperature. Observed (circles), calculated (red line), difference (blue line), and background (green line) are shown, respectively. The ticks indicate the allowed Bragg reflections. (b) (Left) SAED pattern of PNMO along the [010] zone-axis. The extinction diffraction spots appear due to multiple scattering. (Right) Simulated SAED pattern of PNMO along the [010] zone-axis corresponding to the sub-space groups P_1n_1 or P_12/n_1. (c) Crystal structure of PNMO viewed from the *a*-, *b*-, *c*-axis. (d) Scheme of the crystal structure for B-site-ordered double-perovskite PNMO, as shown in a rock salt view. (e) Scheme of NiO_6 and MoO_6 octahedra.

double perovskite, giving rise to multiple and competing magnetic and electrical interactions such as B−B, B′−B′, and B−B′. Recently, much attention has been given to the double perovskites with the general chemical formula $A_2BB'O_6$, owing to their fascinating structural and wide variety of physical properties since the report of room-temperature colossal

https://doi.org/10.1021/acs.chemmater.1c02826
Chem. Mater. 2022, 34, 97−106

magnetoresistance in the double-perovskite Sr_2FeMoO_6.[20] Subsequently, many $A_2BB'O_6$ (A = Ba, Sr, Ca, Pb, and Bi; B/B′ = Fe, Co, Ni, Cr, Mn, and Os) double perovskites with properties such as ferromagnetic, ferroelectric, and multiferroic were synthesized under ambient or high-pressure conditions.[21−25]

Pb is a main-group element with a charge degree of freedom stemming from the possibility of having either the $6s^2$ (Pb^{2+}) or the $6s^0$ (Pb^{4+}) electronic configuration typically found in $PbFeO_3$ ($Pb^{2+}{}_{0.5}Pb^{4+}{}_{0.5}Fe^{3+}O_3$).[26] Their ions are called valence-skipping (or negative-U) ions because the $6s^1$ configuration (Pb^{3+}) is prohibited.[27] Pb-based oxides with a stereo-chemically active lone pair of Pb^{2+} cation have been the subject of long-standing interest due to large remnant polarization and high-temperature structural/electronic transitions, as found in $Pb(Zr,Ti)O_3$. In this work, we prepared the B-site-ordered double-perovskite Pb_2NiMoO_6 (PNMO) at high pressure and high temperature. The crystal structure, valence states, and magnetic properties were investigated with synchrotron X-ray diffraction (SXRD), electron diffraction (ED), X-ray absorption spectrum (XAS), and temperature-dependent magnetic susceptibility (M−T). To the best of our knowledge, PNMO is the first report of an $A_2BB'O_6$-type double perovskite with the low-symmetry space group, *Pc* (no. 7).

EXPERIMENTS

A polycrystalline sample of PNMO was prepared by high pressure and high temperature. The starting materials PbO (Alfa, 99.9995%), MoO_3 (Alfa, 99.9%), and NiO (Alfa, 99.9%) were mixed homogeneously in a molar ratio 2:1:1 and pressed into a pellet with a diameter of 6 mm and height of 3.0 mm in an argon gas-filled glovebox. The pre-pressed pellet was sealed into a gold capsule and then calcined at 1273 K and 5 GPa for half an hour in a cubic-anvil-type high-pressure apparatus. The temperature was quenched to room temperature, before the pressure was released. In this process, brown polycrystalline PNMO was obtained.

The SXRD for PNMO was collected with a large Debye−Scherrer camera installed at the BL02B2 beamline of SPring-8 in Japan with a wavelength of 0.420124 Å. The crystal structure solution was carried out by EXPO2014 software.[28] Temperature-dependent XRD of PNMO measurements has been performed using a Rigaku Ultima VI diffractometer with Cu Kα radiation generated at 40 kV and 40 mA. Diffraction data were collected in the angle (2θ) range from 10 to 120° with steps of 0.01°. The structure refinement was performed by the Rietveld method using the GSAS program.[29] The specimens for transmission electron microscopy were milled and dispersed into high-purity ethanol and transferred on a carbon film with a copper-supporting grid. The selected area ED (SAED) and convergent-beam ED (CBED) patterns were obtained using a CM200 (Philips) transmission electron microscope with a field emission gun at an accelerating voltage of 200 kV. The resistivity of PNMO was measured with the standard four-probe method. The size of the sample was ∼2 × 1 × 1 mm for the electrical measurements. The field dependence of the isothermal magnetization (M−H and M−T) was measured with a quantum design superconducting quantum interference device magnetometer (MPMS3). The valence state of metal ions in PNMO was determined by XAS. The XAS spectra at the Ni-$L_{2,3}$ and Mo-$L_{2,3}$ edges were measured at the TPS45A and TLS16A beamline, respectively, at the National Synchrotron Radiation Research Center in Taiwan. The high-resolution partial fluorescence yield (PFY) Pb-L_3 XAS spectra with an overall resolution of ∼1.0 eV was measured at the ID 20 beamline of the European Synchrotron Radiation Facility in France.[30] The permittivity was measured with different frequency using an Agilent-4980A LCR meter on a solid pellet with 5.2 mm^2 in area and 230 μm in thickness. The ferroelectric hysteresis loops were measured at 100 Hz with a Radiant Precision Premier-II Ferroelectric Test System at different temperatures based on the proposed positive-up negative-down method. The detailed experimental descriptions can be found in the previous literature.[31]

RESULTS AND DISCUSSION

According to the previous report,[32] PNMO possesses cubic symmetry with the lattice parameter a = 3.971 Å. However, our SXRD pattern shows the splitting of the high-angle peaks (see the inset of Figure 1a), thus excluding the possibility of cubic symmetry. Group-theoretical analysis has shown that twelve possible space groups exist in the structures of ordered double-perovskite $A_2BB'O_6$, in which the ordering of cations B and B′ into alternate octahedra is considered as combination with the ubiquitous BO_6 (or $B'O_6$) octahedral tilting.[33] Among the twelve possible groups from the group-theoretical analysis, there are four tetragonal ($P4/mnc$, $P4_2/nnm$, $I4/m$, and $P4_2/n$) and only one orthorhombic ($Pnnn$). The structures with space groups $P4/mnc$ and $I4/m$ have approximate cell dimensions (relative to the edge of the simple perovskite) of $\sqrt{2} \times \sqrt{2} \times 2$, while the structures with space groups $P4_2/nnm$, $P4_2/n$, and $Pnnn$ have approximate cell dimension of 2 × 2 × 2.[33] There are difficulties in the actual structural determination even with a high-quality sample due to the nature of these compounds.[33,34] However, we noted that XRD diffraction peaks of PNMO split near 20.05°(see the inset of Figure 1a) can be used as an indicator for the monoclinic (or triclinic) distortion, as described in the following context. For the double-perovskite tetragonal $\sqrt{2} \times \sqrt{2} \times 2$ cells, only a single (404) peak is possible near 20.05° in the pattern, and similarly, only a single peak (444) is possible for the tetragonal and orthorhombic 2 × 2 × 2 cells. Therefore, the split of the (404) or (444) peak near 20.05° indicates that the structure of the double-perovskite PNMO is neither tetragonal nor orthorhombic. The SXRD pattern of the PNMO sample can be indexed by a monoclinic unit cell with lattice parameters a = 5.6341(6), b = 5.6384(6), c = 9.7523(6) Å, α = 90.00, β = 125.18, and γ = 90.00°. This corresponds to the structure with the space group $P2_1/c$.[33] Then, we tried to solve the structure with EXPO2014 based on SXRD data, and the Rietveld refinement results were R_p = 23.2%, R_{wp} = 24.4%, R_I = 14.7%, and R_F = 24.9%. It seems that the structure model is not very satisfactory. We suspected that this compound may have lower symmetry due to the severe distortion of the NiO_6 and MoO_6 octahedron induced by the lone-pair electron effect of Pb^{2+} ions. Therefore, we tried to solve the structure in space group *Pc* (no. 7, a subgroup of the $P2_1/c$) with lower symmetry. All the R factors (R_p = 9.33%, R_{wp} = 12.9%, R_I = 12.0%, and R_F = 14.2%.) significantly improved. To further confirm the correct space group of PNMO, we performed SAED and CBED experiments. According to the SAED results along the [010] zone-axis (see Figure 1b), we found that if PNMO belongs to the space group *Pc* (no. 7), only the sub-space group P_1n_1 can satisfy the extinction rules. On the other hand, if PNMO belongs to the space group *P*2/c (no. 13), only the sub-space group P_12/n_1 can satisfy the extinction rules. The symmetry operations of *Pc* include (1) 1; (2) c x, 0, z, while the symmetry operations of *P*2/*c* include (1)1; (2) 2 0, y, 1/4; (3) −1 0, 0, 0; (4) c x, 0, z. Therefore, the difference between space groups *Pc* and *P*2/*c* is whether there are twofold axes along the [010] zone-axis. Our CBED pattern along the [010] zone-axis indicates that there is no twofold axis along the [010] zone-axis (see Figure S1). Thus, we can confirm that the space group *Pc* is the correct choice for the PNMO structure. Finally,

https://doi.org/10.1021/acs.chemmater.1c02826
Chem. Mater. 2022, 34, 97−106

the Rietveld structure refinement was performed using the GSAS program.[29] The SXRD Rietveld structural refinement result for PNMO is shown in Figure 1a. The detailed refined structure parameters are listed in Table 1. Figure 1c illustrates

Table 1. Crystallographic Parameters of PNMO Refined from the SXRD Pattern at RT[a]

atom	site	x	y	z	100 × B_{iso} (Å)
Pb1	2a	0.6212(9)	0.7921(4)	0.6503 (4)	1.36(9)
Pb2	2a	0.1221 (1)	0.7926 (4)	0.1508 (3)	1.17(8)
Ni1	2a	−0.1289 (5)	1.2593 (8)	−0.0989 (2)	0.44(4)
Mo1	2a	0.3839 (7)	1.2814 (7)	0.4103 (7)	0.79(0)
O1	2a	1.1394 (0)	0.5065 (2)	0.8869 (6)	1.40(1)
O2	2a	0.6685 (6)	0.4966 (2)	0.4016 (5)	0.41(2)
O3	2a	0.6098 (3)	1.2406 (7)	0.6392 (9)	2.92(8)
O4	2a	0.1534 (1)	1.2013 (8)	0.1885 (4)	0.86(6)
O5	2a	0.6361 (6)	1.0206 (3)	0.4343 (8)	0.82(4)
O6	2a	0.1361 (7)	1.0135 (6)	−0.0724 (5)	0.22(4)

[a]Space group *Pc* (no. 7), Z = 2, a = 5.6341(6) Å, b = 5.6384(6) Å, c = 9.7523(6) Å, α = 90.00°, β = 125.18°, γ = 90.00°, ρ_{cal} = 8.722(3) g/cm^3, V = 253.2(0) Å^3, R_{wp} = 8.12%, and R_p = 5.81%.

the crystal structure of PNMO viewed along the *a*-, *b*-, and *c*-axis, respectively. The NiO_6 and MoO_6 octahedra are grossly distorted. The average octahedral tilt angle is defined as $\psi = (180 - \phi)/2 = 6.59°$, where ϕ is the inter-octahedral Ni−O−Mo angle. PNMO displays a significantly larger structural distortion compared with that of Sr_2NiMoO_6 ($\psi = 2.87°$).[14,18] The Ni and Mo ions in PNMO are ordered in a rock-salt-type manner (Figure 1d). No anti-site disordering was found, as expected, due to the large differences of charge and effective ionic radius of Mo^{6+} (0.59 Å) and Ni^{2+} (0.69 Å).[35] No anomaly was observed in the occupational parameters at any atomic sites. Full occupancy of the oxygen sites was observed as well. Thus, PNMO, the ordered perovskite, should have a stoichiometric composition. The rare ABO_3-type simple perovskite $CuNbO_3$ with the monoclinic space group *Pc* and $AA'BB'O_6$-type perovskite $SrLaCuNbO_6$ with the triclinic space group *P*-1 have been reported in previous studies.[36,37] However, to the best of our knowledge, PNMO is the first report of B-site-ordered double perovskite with such a low-symmetry space group, *Pc*. The Pb−O, Ni−O, and Mo−O bond lengths are summarized in Table 2. Bond valence sum (BVS) calculations[38] based on SXRD refinement confirm that the valence states are +1.98 for Pb1, +2.21 for Pb2, +2.14 for Ni, and +5.98 for Mo, respectively. Therefore, the formal oxidation states of PNMO are $Pb_2^{2+}Ni^{2+}Mo^{6+}O_6$, which is consistent with XAS results described below.

As mentioned above, the NiO_6 and MoO_6 octahedra in PNMO are strongly distorted from ideal symmetry (see Figure 1e). The relative distortion of BO_6 octahedra in perovskites can be estimated by the magnitude of Δ in the formula $\Delta = \frac{1}{6}\sum_{i=1}^{6}\left(\frac{d_i - d_{av}}{d_{av}}\right)^2$, where d_i is the individual B−O bond length and d_{av} is the average bond length.[5] The distortion parameter, Δ, of NiO_6 and MoO_6 for PNMO is 6.74 × 10^{-3} and 7.37 × 10^{-3}, respectively. These values are much larger than those for Ba_2NiMoO_6 and Sr_2NiMoO_6 (see Table 3), which have the same valence distribution as PNMO. Moreover, as the ionic size of Sr^{2+}, Pb^{2+}, and Ba^{2+} gradually increases from 1.44 to 1.49 to 1.61 Å, respectively, the symmetry of the corresponding

Table 2. Pb−O, Ni−O, and Mo−O Bond Lengths and BVSs[a] for PNMO Refined from the SXRD Pattern at RT

	Pb1	Pb2	Ni1	Mo1
O1	2.961(0)	2.810(5)	2.118(2)	1.737(0)
	2.945(6)	3.086(1)		
O2	2.824(4)	2.817(5)	1.789(3)	2.051(1)
	3.077(9)	3.093(3)		
O3	2.530(6)	2.829(1)	2.089(1)	1.839(0)
	3.110(7)	2.820(6)		
O4	2.867(3)	3.347(5)	2.314(6)	1.825(5)
	2.800(2)	2.324(5)		
O5	2.920(1)	2.529(7)	2.201(1)	1.963(0)
	2.511(2)	2.908(1)		
O6	2.558(7)	2.869(8)	1.942(8)	2.239(3)
	2.871(3)	2.549(3)		
BVS	1.98	2.21	2.14	5.98

[a]$V_i = \sum_j S_{ij}$, $S_{ij} = \exp[(r_0 - r_{ij})/0.37]$. Values calculated using r_0 = 2.112 for Pb^{2+}, 1.654 for Ni^{2+}, and 1.907 for Mo^{6+}.

Table 3. Ionic Radius of A-Site r_A, Average A−O, Ni−O, and Mo−O Bond Distance, Distortion Δ of NiO_6 and MoO_6, BVS Values, and AFM Transition Temperature (T_N) for Ba_2NiMoO_6, Sr_2NiMoO_6, PNMO, and $PbNiO_3$, Respectively

	Ba_2NiMoO_6	Sr_2NiMoO_6	Pb_2NiMoO_6	$PbNiO_3$
space group	$Fm\bar{3}m$	$I4/m$	Pc	$Pnma$
r_A/Å	1.61	1.44	1.49	1.49
⟨A−O⟩	2.846(9)	2.783(1)	2.832(1)	2.407(0)
			2.831(5)	
⟨Ni−O⟩	2.097(2)	2.024(4)	2.075(8)	2.076(0)
⟨Mo−O⟩	1.927(2)	1.921(4)	1.942(4)	
ΔNiO_6	0	8.07 × 10^{-6}	6.74 × 10^{-3}	7.18 × 10^{-5}
ΔMoO_6	0	3.68 × 10^{-6}	7.37 × 10^{-3}	
BVS (A)	2.66	2.08	1.98	4.11
			2.20	
BVS (Ni)	1.81	2.21	2.14	1.92
BVS (Mo)	5.70	5.78	5.97	
T_N/K	64	81	26	225

crystal structure is expected to change gradually. However, the symmetry of PNMO is lower than that of Sr_2NiMoO_6 and Ba_2NiMoO_6. The most obvious difference between these three compounds is that the A-site ion of PNMO, Pb^{2+}, has $6s^2$ lone pair electrons. Therefore, the low symmetry and large distortions of the NiO_6 and MoO_6 octahedra in PNMO are mainly due to the steric effect of the $6s^2$ lone pair electrons. Moreover, we noticed the simple perovskite-type compound $PbNiO_3$[5], in which the valence state of the Pb ion is +4 and without lone pair, showing a 2-orders of magnitude smaller (Δ = 7.20 × 10^{-5}) for NiO_6 distortion than that of PNMO. These results corroborate that the low symmetry and large distortion of NiO_6 and MoO_6 in PNMO originate from the steric effect by the lone pair electrons. The large distortion of NiO_6 and MoO_6 octahedra greatly affect the magnetism of PNMO, as discussed below.

It is well known that the energy position and the multiple spectral features XAS at the 3d transition-metal $L_{2,3}$ edges are very sensitive to the valence and the local environment.[39,40] The same energy position and the very similar spectral feature of PNMO and NiO at the Ni-$L_{2,3}$ edge in Figure 2a indicate a clear Ni^{2+} valence state with an octahedral local coordination in PNMO. Different from 3d elements, the detailed spectral

https://doi.org/10.1021/acs.chemmater.1c02826
Chem. Mater. 2022, 34, 97−106

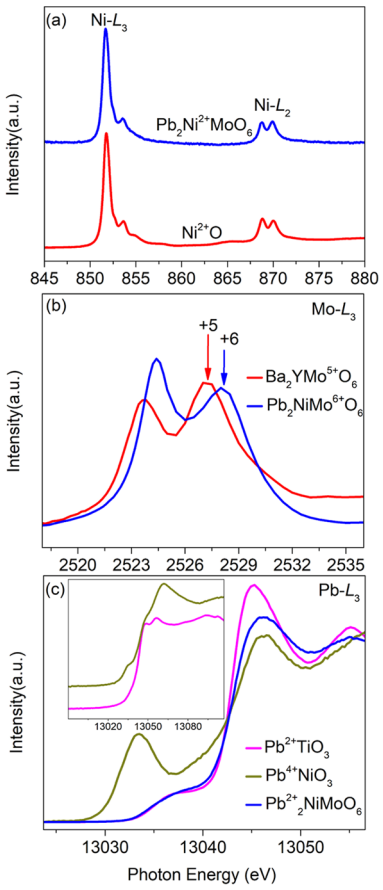

Figure 2. XAS spectra at (a) Ni-$L_{2,3}$ edge of PNMO and NiO (as a Ni^{2+} reference). (b) Mo-L_3 edges of PNMO and Ba_2YMoO_6 (as a Mo^{5+} reference). (c) Pb-L_3 edge of PNMO and $PbTiO_3$ (as a Pb^{2+} reference) and $PbNiO_3$ (as a Pb^{4+} reference). The inset shows Pb-L_3 XAS spectra of PNMO and $PbNiO_3$ taken with the conventional transmission mode.

feature of the XAS spectrum at 4*d* transition metal $L_{2,3}$ edge is mainly determined by the crystal field splitting, while an increase in the valence state of 4d transition-metal ion by one causes a shift of the t_{2g}- and e_g-related peaks at the L_3 XAS spectra by about 1 eV toward higher energies.[41−44] To determine the oxidation state of Mo ions precisely in PNMO, the Mo-L_3 XAS spectrum for PNMO was measured. Figure 2b shows the Mo-L_3 XAS of PNMO together with that of Ba_2YMoO_6 as a Mo^{5+} reference.[45] The higher energy shift of the Mo-L_3 XAS spectra of PNMO, relative to that of $Ba^{2+}{}_2Y^{3+}Mo^{5+}O_6$, indicates a Mo^{6+} valence state in PNMO. Figure 2c presents the PFY Pb-L_3 XAS spectrum of PNMO together with $PbTiO_3$ (as a Pb^{2+} reference) and $PbNiO_3$ (as a Pb^{4+} reference), respectively. Unlike the XAS spectra of 3d and 4d transition metals at *L* and *K* edges, where the energy positions are very sensitive to the number of the localized d valence electrons, at the Pb-*L* edge, the 6s electrons represent the valence state of Pb ions. However, the Pb 6s- and Pb 6d-related features strongly overlap at the Pb-L_3 in the traditional transmission mode, due to a large life time broadening and poor experimental resolution.[46] Fortunately, the Pb-L_3 XAS spectra taken from the high-resolution PFY mode provide an opportunity to identify the spectral feature of the Pb 6*s* state.[47,48] As shown in Figure 2c, a sharp pre-edge peak at 13,030 eV in the Pb-L_3 XAS spectrum for the Pb^{4+} reference $PbNiO_3$ can be assigned to the dipole-allowed transition from the $2p_{3/2}$ core level to the unoccupied 6*s* states with two 6*s* holes. In the case of $PbTiO_3$, the pre-edge peak is absent due to the fully occupied 6s state. Figure 2c shows that PNMO has a Pb-L_3 XAS profile similar to that of the Pb^{2+} reference $PbTiO_3$. No pre-edge peak is observed, demonstrating the valence state of Pb ions with fully occupied $6s^2$ state. The XAS results indicate that the formal valence states in PNMO are $Pb^{2+}{}_2Ni^{2+}Mo^{6+}O_6$. The inset of Figure 2c shows the Pb-L_3 XAS spectra of $PbTiO_3$ and $PbNiO_3$ in the transmission mode, where the 6s-related peak for the Pb^{4+} state in $PbNiO_3$ is a poorly resolved broad shoulder. This result is consistent with the BVS calculations based on the SXRD refinement. As summarized in Table 3, PNMO has the same valence distribution as Sr_2NiMoO_6 and Ba_2NiMoO_6 ($A^{2+}{}_2Ni^{2+}Mo^{6+}O_6$).

Next, we focus on the electrical transport property of PNMO. Figure 3 shows the temperature dependence of

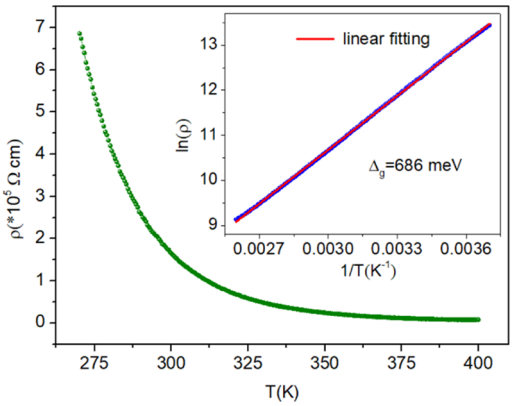

Figure 3. Temperature dependence of resistivity for PNMO. The inset shows the $\ln(\rho)$ as a function of inverse temperature and its linear fitting between 270 and 380 K.

resistivity for the PNMO sample, which exhibits semiconducting behavior same as Sr_2NiMoO_6.[49] The resistivity of PNMO is about 1.67×10^5 Ω cm at 300 K. The inset presents the linear fit to the curve of $\ln(\rho)$ as a function of inverse temperature using the formula of $\rho \propto \exp(\Delta_g/2k_BT)$, where Δ_g is the semiconducting band gap and k_B is the Boltzmann constant. The resistivity curve can be well fitted, and the band gap Δ_g of PNMO is evaluated to be ∼686 meV.

The temperature dependence of magnetic susceptibility χ for PNMO, as shown in Figure 4a, indicates unusual two-step antiferromagnetic (AFM) transitions: the first at 18 K and the second at 26 K are seen in a magnified view of the temperature-dependent $d\chi/dT$ (see the inset of Figure 4a) and in the temperature-dependent specific heat (see Figure 5a). Similar two-step AFM has also been observed in mixed A-site and B-site charge-ordered quadruple perovskite $Pb^{2+}Pb^{4+}{}_3Co^{2+}{}_2Co^{3+}{}_2O_{12}$ (PCO) with B-site Co^{2+} ion with high spin $S = 3/2$ and B′-site Co^{3+} ion with low spin $S = 0$.[50] The magnetic interaction in PCO is mediated by a $Co^{2+}-O-Co^{3+}-O-Co^{2+}$ path.[50] The magnetic Co^{2+} ions at the special positions of a cubic cell form a regular FCC lattice with strong geometrical frustrations expected.[51] The magnetic interaction of PNMO is very similar to that of PCO. In PNMO, the Mo^{6+} ion with $4d^0$ electronic configuration has no magnetic moment,[45] and the magnetic exchange is mainly via the $Ni^{2+}-O-Mo^{6+}-O-Ni^{2+}$ pathways.[21,52] Because there are

https://doi.org/10.1021/acs.chemmater.1c02826
Chem. Mater. 2022, 34, 97−106

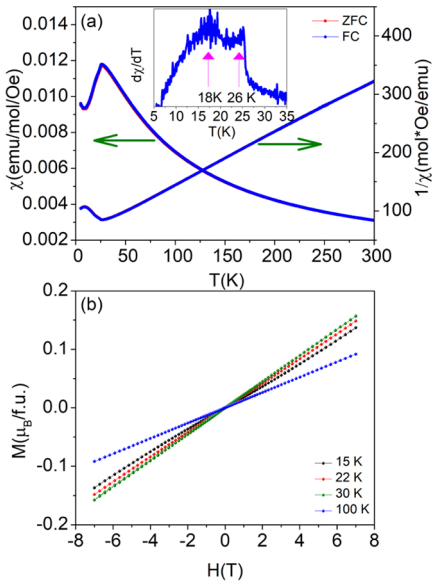

Figure 4. (a) Temperature dependence of magnetic susceptibility χ and Curie–Weiss fitting for PNMO. The external magnetic field is 0.1 T. The inset shows a magnified view of the $d\chi/dT$ vs T (K) at low temperature. (b) Field-dependent magnetization of PNMO at various temperatures.

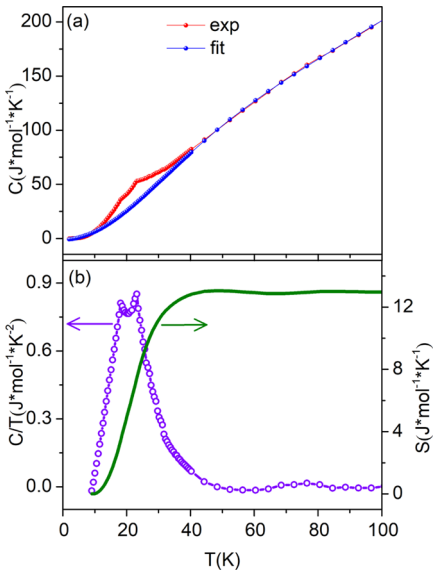

Figure 5. (a) Temperature dependence of specific heat for PNMO. The blue curve shows the fit of lattice specific heat. (b) C_p/T vs T and the numerical integration of the entropy S after subtracting the lattice specific heat around T_N for PNMO.

multiple competing magnetic super-exchange interactions induced by the geometrical frustration of Ni^{2+} (d^8, $S = 1$) in PNMO, unusual two-step AFM transitions occurred. The $\chi(T)$ data above the second-transition temperature of 26 K can be well fitted with the Curie–Weiss law. The obtained Curie constant is $C = 1.10$ emu K mol^{-1} Oe^{-1}, and the Weiss temperature is $\theta_w = -59.6$ K; the negative θ_w verifies the AFM interactions. According to the Curie constant, the effective magnetic moment (μ_{eff}) is calculated to be 2.97 μ_B/Ni^{2+} for PNMO. The μ_{eff} value is close to that expected for the spin-only theoretical value (2.83 μ_B) for the Ni^{2+} ion with high-spin configuration ($S = 1$).[5] The discrepancy is thought to be due to spin–orbit interactions. Furthermore, Figure 3b shows M–H for PNMO measured at 15, 22, 30, and 100 K, just below and above the AFM transition temperature, T_N, respectively. The magnetization is linearly dependent on the applied magnetic field; no open magnetic hysteresis loop is observed in PNMO, which indicates that no canted ferromagnetism accompanies the AFM transition.

As mentioned above, the Mo^{6+} ion does not carry any magnetic moment, so the magnetic exchange in PNMO is mainly via the Ni^{2+}–O–Mo^{6+}–O–Ni^{2+} bonds.[21,52] In contrast, the AFM interactions in $PbNiO_3$ are strengthened by the super-exchange interaction between Ni ions via oxygen (Ni^{2+}–O–Ni^{2+} path).[5] Thus, the T_N of all the A_2NiMoO_6 (A = Ba, Sr, and Pb) is much lower than that of $PbNiO_3$, in agreement with the above considerations.[50] The slightly higher observed for Sr_2NiMoO_6 ($T_N = 81$ K) with respect to that of Ba_2NiMoO_6 ($T_N = 64$ K) implies the presence of stronger magnetic interactions for the former. The strength of the magnetic interactions is related to the Ni–O bond distances, which is significantly shorter in Sr_2NiMoO_6 than that in PNMO, and accounts for the stronger overlap between the Ni 3d and O 2p orbitals in Sr_2NiMoO_6, thus enhancing the super-exchange process and giving rise to the AFM order at the higher T_N in Sr_2NiMoO_6.[14] However, the average ⟨Ni–O⟩ bond length of PNMO is shorter than that of Ba_2NiMoO_6, the T_N of PNMO is only 26 K versus 64 K of Ba_2NiMoO_6. The main reason for the difference in T_N is the large distortion of the Ni^{2+}–O–Mo^{6+} angle ϕ in PNMO from the ideal 180° (≈157.4–170.4°), which is deleterious for optimal 3d–2p overlap.

Figure 5a shows the temperature dependence of specific heat for PNMO without an external magnetic field. The anomalies at 18 and 26 K support the transitions of long-rang magnetic ordering in PNMO. In order to estimate the entropy release associated with AFM ordering, the lattice contribution has been calculated and subtracted from the total specific heat. For this purpose, we fitted the lattice contribution with the Einstein model (see the blue curve in Figure 5a).[53,54] Figure 5b shows C_p/T versus T and the magnetic entropy $S_{mag} = \int_{T1}^{T2}(C_{mag}/T)dT$ for PNMO. The magnetic entropy increases with temperature and nearly saturates just above $T_N = 26$ K with a value of 12.95 J mol^{-1} K^{-1}. In PNMO, the magnetic structure can be described by the ordered Ni spins (Ni^{2+}, d^8, $S = 1$). The Ni^{2+} ions carry two holes with spin $S = 1$ in the 3d shell. Therefore, the value of magnetic entropy is expected with R*ln $(2S + 1)$ = 9.13 J mol^{-1} K^{-1} for a $S = 1$ system. The theoretical value is consistent with the experimentally obtained S_{mag}, which confirms the bulk nature of AFM order in PNMO.

Temperature-induced structural transformation is usually observed in Pb-based oxides, such as $PbTiO_3$, $PbNiO_3$, and so forth. Specifically, phase transition from tetragonal, $I4/m$ to cubic, $Fm\bar{3}m$ was observed at 550 K for analogous compound Sr_2NiMoO_6.[55] In order to examine the possible phase transition, we investigated the temperature-dependent XRD for PNMO from 298 to 433 K. Figure 6a shows an obvious phase transition between 393 and 413 K in PNMO. Figure 6b shows the comparison of XRD patterns for PNMO between 298 and 433 K. Compared with the XRD pattern obtained at 298 K, many diffraction peaks disappeared in the XRD pattern obtained at 433 K, which indicate that the crystal structure of PNMO changes from low symmetry to high symmetry at 393–413 K. The XRD pattern at 433 K can be indexed well with the

https://doi.org/10.1021/acs.chemmater.1c02826
Chem. Mater. 2022, 34, 97–106

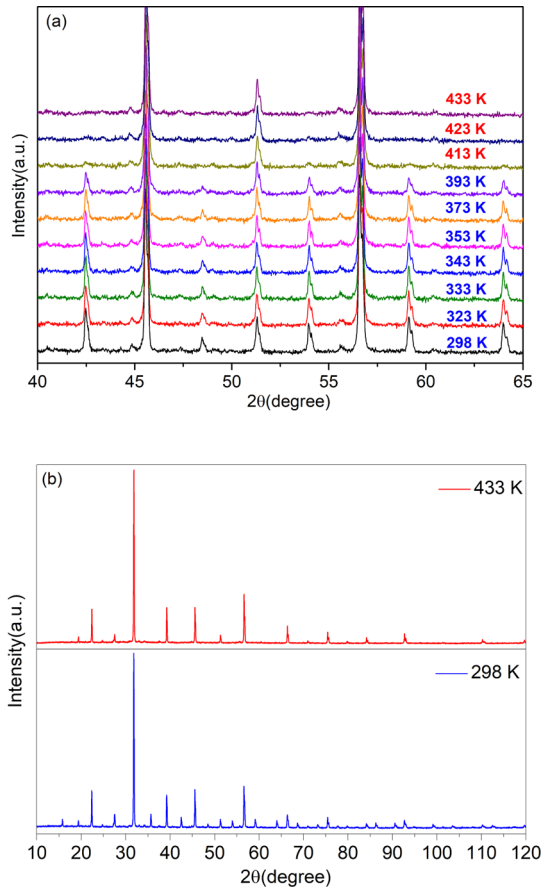

Figure 6. (a) Temperature-dependent XRD patterns for PNMO obtained from 298 to 433 K. The obvious phase transition occurred between 393 and 413 K. (b) Comparison of XRD patterns for PNMO at 298 and 433 K.

space group $Fm\bar{3}m$. The Rietveld structural refinement result is shown in Figure 7. The inset of Figure 7 shows the crystal structure of PNMO with the space group $Fm\bar{3}m$. The detailed

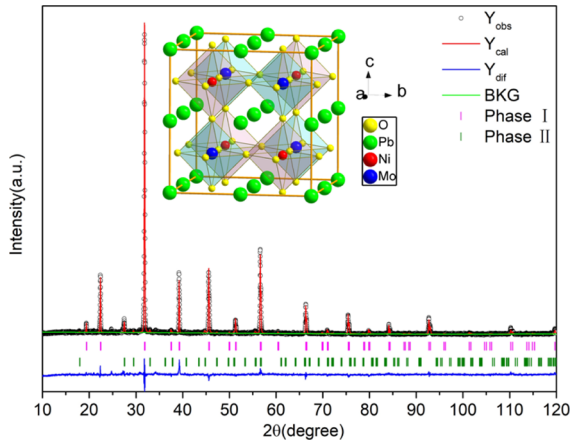

Figure 7. Rietveld refinements of XRD patterns for PNMO at 433 K. Observed (crosses), calculated (red), difference (blue), and background (green) are shown in the figure, respectively. The ticks indicate the allowed Bragg reflections with the space group $Fm\bar{3}m$ (phase I: PNMO, ~95.6 wt %) and $I41/a$ (phase II: $PbMoO_4$, ~4.4 wt %). The inset shows the refined crystal structure of $Fm\bar{3}m$ PNMO at 433 K.

refined structural parameters of PNMO at 433 K are listed in Table 4. BVS results based on XRD refinement show that the

Table 4. Refined Structure Parameters of PNMO Based on XRD Data Collected at 433 K[a,b]

	XRD
a (Å)	7.9737(2)
Z	4
formula weight (g/mol) (g/mol)	665.03
cacl. density (g/cm^3)	8.7124(6)
V (Å^3)	506.97(1)
O_x	0.2425(1)
U_{iso} (Pb) (Å2)	0.0507(4)
U_{iso} (Ni) (Å2)	0.0426(5)
U_{iso} (Mo) (Å2)	0.0237(7)
U_{iso} (O) (Å2)	0.0158(9)
Pb−O (×12) (Å)	2.819(7)
Ni−O (×6) (Å)	2.053(9)
Mo−O (×6) (Å)	1.934(9)
∠Ni−O−Mo (deg)	180
BVS (Pb)	1.77
BVS (Ni)	2.04
BVS (Mo)	5.56
R_{wp} (%)	6.09
R_p (%)	4.58
χ^2	1.902

[a]The BVS values (V_i) were calculated using the formula $V_i = \Sigma_j S_{ij}$ and $S_{ij} = \exp[(r_0 - r_{ij})/0.37)]$. In PNMO, r_0 = 2.112 for Pb^{2+}, 1.654 for Ni^{2+}, and 1.907 for Mo^{6+}. [b]Space group: $Fm\bar{3}m$; atomic sites: Pb 8*c* (0.25, 0.25, 0.25), Ni 4*b* (0.5, 0.5, 0.5), Mo 4*a* (0, 0, 0), and O 24*e* (0.2425, 0, 0).

valence states are +1.77 for Pb, +2.04 for Ni, and +5.56 for Mo, respectively. Therefore, the valence state of PNMO at 433 K is also $Pb_2^{2+}Ni^{2+}Mo^{6+}O_6$, the same as the BVS results based on SXRD obtained at room temperature. The relatively smaller valence of cations at 433 K (relative to those at room temperature) is attributed to the enhancement of bond lengths due to thermal expansion. All the above results show that PNMO undergoes a symmetry-breaking phase transition from a high-temperature centrosymmetric, cubic $Fm\bar{3}m$ phase to a low-temperature non-centrosymmetric, monoclinic Pc phase at 393−413 K.

Since Pc is a polar space group, PNMO may exhibit interesting dielectric/ferroelectric properties. The permittivity $\varepsilon_r(T)$ and dielectric loss $\delta(T)$ measured with different frequencies from 2 to 380 K are shown in Figure S2, respectively. Interestingly, the dielectric loss $\delta(T)$ remains at a very low value (<0.02), and the relative dielectric constant $\varepsilon_r(T)$ is almost constant (~50) at all frequencies when the temperature is below 30 K, which indicate the intrinsic dielectric property of PNMO in the low-temperature range. However, as the temperature increased to 50 K, the $\varepsilon_r(T)$ of PNMO quickly increases and shows frequency-independent to frequency-dependent translation accompanied with enhanced dielectric loss from 0.01 to 0.5, indicating the presence of leakage currents at temperatures above 50 K. No anomalous peak is observed in the dielectric constant $\varepsilon_r(T)$ in the whole measured temperature range. To examine the possible ferroelectricity of PNMO, we measured the polarization versus electric field (P−E) at 300 and 20 K under selected electric fields (see Figure S3). No P−E hysteresis loops were observed

https://doi.org/10.1021/acs.chemmater.1c02826
Chem. Mater. 2022, 34, 97−106

in PNMO even when the electric field increased to 15 kV/cm. The absence of ferroelectricity in PNMO may be due to the polycrystalline sample with randomly distributed grains. Another reason may be due to the grain boundary effect and leaking current issue, preventing the application of maximum electric fields in the experiment since PNMO shows a large dielectric loss $\delta(T)$ (~0.5) when the temperature is above 50 K. The relatively large dielectric loss $\delta(T)$ at high temperature is consistent with the semiconducting behavior of PNMO.

CONCLUSIONS

Pb_2NiMoO_6, a B-site-ordered double perovskite, was synthesized under high pressure and high temperature. Refinement of synchrotron powder X-ray diffraction data shows that Pb_2NiMoO_6 crystallizes in the low-symmetry monoclinic space group, *Pc* (no. 7). Structural analysis shows that NiO_6 and MoO_6 octahedra are ordered in a rock-salt-type arrangement and are tilted with large distortions. XAS results combined with BVS calculations confirm the valence distribution in PNMO as $Pb_2^{2+}Ni^{2+}Mo^{6+}O_6$. The magnetic and specific heat characterizations reveal unusual two-step AFM transitions, at 18 and 26 K. Comparing the A_2NiMoO_6 (A = Sr, Pb, and Ba) analogues, the ionic size of the A site ion increases from Sr^{2+} (1.44 Å) to Pb^{2+}(1.49 Å) to Ba^{2+} (1.61 Å), while the symmetry and T_N change from tetragonal, *I*4/*m* and 81 K to monoclinic, *Pc* and 26 K to cubic, $Fm\bar{3}m$, and 64 K, respectively. A temperature-induced structural phase transition from polar monoclinic *Pc* phase to non-polar $Fm\bar{3}m$ phase was observed around 400 K. The low symmetry and T_N observed for Pb_2NiMoO_6 are attributed to the large distortion of NiO_6 and MoO_6 octahedra induced by the lone pair electron effect of Pb^{2+} with $6s^2$ electronic configuration. These results have guiding significance for designing and searching new functional materials with stereo-chemically active lone pair cations.

ASSOCIATED CONTENT

Supporting Information

The Supporting Information is available free of charge at https://pubs.acs.org/doi/10.1021/acs.chemmater.1c02826.

CBED patterns of Pb_2NiMoO_6 along the [010] zone-axis; temperature dependence of relative dielectric constant ε_r and dielectric loss for Pb_2NiMoO_6; and polarization versus electric field (P–E) of Pb_2NiMoO_6 measured at 300 K and 20 K under selected electric fields (PDF)

AUTHOR INFORMATION

Corresponding Authors

Runze Yu − *Beijing National Laboratory for Condensed Matter Physics, Institute of Physics, Chinese Academy of Sciences, Beijing 100190, China; Institute of Solid State Chemistry University of Science and Technology Beijing, Beijing 100083, China;* orcid.org/0000-0001-9889-0299; Email: yurz@iphy.ac.cn

Zhiwei Hu − *Max-Planck Institute for Chemical Physics of Solids, Dresden 01187, Germany;* orcid.org/0000-0003-0324-2227; Email: Zhiwei.Hu@cpfs.mpg.de

Changqing Jin − *Songshan Lake Materials Laboratory, Dongguan 523808, China; Beijing National Laboratory for Condensed Matter Physics, Institute of Physics, Chinese Academy of Sciences, Beijing 100190, China; School of Physics Sciences, University of Chinese Academy of Sciences, Beijing 100190, China*; Email: Jin@iphy.ac.cn

Authors

Jianfa Zhao − *Songshan Lake Materials Laboratory, Dongguan 523808, China; Beijing National Laboratory for Condensed Matter Physics, Institute of Physics, Chinese Academy of Sciences, Beijing 100190, China;* orcid.org/0000-0002-7507-9441

Xiao Wang − *Max-Planck Institute for Chemical Physics of Solids, Dresden 01187, Germany*

Xi Shen − *Beijing National Laboratory for Condensed Matter Physics, Institute of Physics, Chinese Academy of Sciences, Beijing 100190, China;* orcid.org/0000-0003-4677-2455

Christoph J. Sahle − *ESRF, Grenoble Cedex 9 38043, France;* orcid.org/0000-0001-8645-3163

Cheng Dong − *Peking University Shenzhen Graduate School, School of Advanced Materials, Shenzhen 518055, China*

Hajime Hojo − *Department of Advanced Materials Science and Engineering, Faculty of Engineering Sciences, Kyushu University, Kasuga, Fukuoka 816-8580, Japan;* orcid.org/0000-0001-6727-8435

Yuki Sakai − *Kanagawa Institute of Industrial Science and Technology (KISTEC), Ebina 243-0435, Japan; Laboratory for Materials and Structures, Tokyo Institute of Technology, Yokohama 226-8503, Japan;* orcid.org/0000-0002-8427-4740

Jun Zhang − *Beijing National Laboratory for Condensed Matter Physics, Institute of Physics, Chinese Academy of Sciences, Beijing 100190, China;* orcid.org/0000-0002-9980-9074

Wenmin Li − *Beijing National Laboratory for Condensed Matter Physics, Institute of Physics, Chinese Academy of Sciences, Beijing 100190, China*

Lei Duan − *Beijing National Laboratory for Condensed Matter Physics, Institute of Physics, Chinese Academy of Sciences, Beijing 100190, China; School of Materials Science and Engineering, Henan University of Technology, Zhengzhou 450007, China;* orcid.org/0000-0002-1254-0317

Ting-Shan Chan − *National Synchrotron Radiation Research Center, Hsinchu, Taiwan 30076, R.O.C*

Chien-Te Chen − *National Synchrotron Radiation Research Center, Hsinchu, Taiwan 30076, R.O.C*

Johannes Falke − *Max-Planck Institute for Chemical Physics of Solids, Dresden 01187, Germany*

Cheng-En Liu − *Max-Planck Institute for Chemical Physics of Solids, Dresden 01187, Germany; Department of Electrophysics, National Yang Ming Chiao Tung University (NYCU), Hsinchu 30010 Taiwan, R.O.C*

Chang-Yang Kuo − *National Synchrotron Radiation Research Center, Hsinchu, Taiwan 30076, R.O.C; Department of Electrophysics, National Yang Ming Chiao Tung University (NYCU), Hsinchu 30010 Taiwan, R.O.C*

Zheng Deng − *Beijing National Laboratory for Condensed Matter Physics, Institute of Physics, Chinese Academy of Sciences, Beijing 100190, China*

Xiancheng Wang − *Beijing National Laboratory for Condensed Matter Physics, Institute of Physics, Chinese Academy of Sciences, Beijing 100190, China;* orcid.org/0000-0001-6263-4963

Richeng Yu − *Beijing National Laboratory for Condensed Matter Physics, Institute of Physics, Chinese Academy of*

https://doi.org/10.1021/acs.chemmater.1c02826
Chem. Mater. 2022, 34, 97−106

Sciences, Beijing 100190, China; School of Physics Sciences, University of Chinese Academy of Sciences, Beijing 100190, China; orcid.org/0000-0002-8086-0910

Martha Greenblatt − *Department of Chemistry and Chemical Biology, Rutgers, The State University of New Jersey, Piscataway, New Jersey 08854, United States;* orcid.org/0000-0002-1806-2766

Complete contact information is available at: https://pubs.acs.org/10.1021/acs.chemmater.1c02826

Notes

The authors declare no competing financial interest.

■ ACKNOWLEDGMENTS

The work was supported by the National Science Foundation and Ministry of Science and Technology of China through the research projects (2017YFA0302900; 2018YFA0305700; 11820101003; 11921004; U2032220; 22171283)and Beijing Nature Science Foundation(2202059). We acknowledge support from the Max Planck-POSTECH-Hsinchu Center for Complex Phase Materials. We also acknowledge the ESRF for provision of synchrotron radiation facilities and technical support.

■ REFERENCES

(1) Goodenough, J.; Longo, J. Crystallographic and magnetic properties of perovskite and perovskite related compounds. *Landolt-Bornstein Numerical Data and Functional Relationships in Science and Technologym*; Hellwege, K.-H., Hellwege, A. M., Eds.; Springer: Berlin, 1970; Vol. *III/4*,10 pp 126−314.

(2) Goodenough, J.; Kafalas, J.; Longo, J. Preparative methods in solid state chemistry. *High Pressure Synthesis*; Academic Press Amsterdam, 1972.

(3) Jin, C.-Q.; Wu, X.-J.; Laffez, P.; Tatsuki, T.; Tamura, T.; Adachi, S.; Yamauchi, H.; Koshizuka, N.; Tanaka, S. Superconductivity at 80 K in $(Sr,Ca)_3Cu_2O_{4+\delta}Cl_{2-y}$ induced by apical oxygen doping. *Nature* **1995**, *375*, 301−303.

(4) Jin, C.-Q.; Adachi, S.; Wu, X.-J.; Yamauchi, H.; Tanaka, S. 117 K Superconductivity in the Ba-Ca-Cu-O System. *Physica C* **1994**, *223*, 238−242.

(5) Inaguma, Y.; Tanaka, K.; Tsuchiya, T.; Mori, D.; Katsumata, T.; Ohba, T.; Hiraki, K.-i.; Takahashi, T.; Saitoh, H. Synthesis, structural transformation, thermal stability, valence state, and magnetic and electronic properties of $PbNiO_3$ with perovskite- and $LiNbO_3$-type Structures. *J. Am. Chem. Soc.* **2011**, *133*, 16920−16929.

(6) Zhang, L.; Chen, J.; Fan, L.; Diéguez, O.; Cao, J.; Pan, Z.; Wang, Y.; Wang, J.; Kim, M.; Deng, S.; Wang, J.; Wang, H.; Deng, J.; Yu, R.; Scott, J. F.; Xing, X. Giant polarization in super-tetragonal thin films through interphase strain. *Science* **2018**, *361*, 494−497.

(7) Yu, R.; Hojo, H.; Watanuki, T.; Mizumaki, M.; Mizokawa, T.; Oka, K.; Kim, H.; Machida, A.; Sakaki, K.; Nakamura, Y.; Agui, A.; Mori, D.; Inaguma, Y.; Schlipf, M.; Rushchanskii, K. Z.; Ležaić, M.; Matsuda, M.; Ma, J.; Calder, S.; Isobe, M.; Ikuhara, Y.; Azuma, M. Melting of Pb charge glass and simultaneous Pb-Cr charge transfer in $PbCrO_3$ as the origin of volume collapse. *J. Am. Chem. Soc.* **2015**, *137*, 12719−12728.

(8) Jin, C.-Q.; Zhou, J.-S.; Goodenough, J. B.; Liu, Q. Q.; Zhao, J. G.; Yang, L. X.; Yu, Y.; Yu, R. C.; Katsura, T.; Shatskiy, A.; Ito, E. High-pressure synthesis of the cubic perovskite $BaRuO_3$ and evolution of ferromagnetism in $ARuO_3$ (A= Ca, Sr, Ba) ruthenates. *Proc. Natl. Acad. Sci. U.S.A.* **2008**, *105*, 7115−7119.

(9) Dai, J.; Shen, X.; Liu, Z.; Zhao, Q.; Wang, X.; Dong, C.; Bian, Y.; Ding, W.; Sheng, Z.; Azuma, M.; Long, Y. Formation of ZnO_4 tetrahedra and ZnO_6 octahedra in $TeZnO_3$ synthesized under high pressure. *Inorg. Chem.* **2018**, *57*, 6716−6721.

(10) Howard, C. J.; Stokes, H. T. Structures and phase transitions in perovskites-a group-theoretical approach. *Acta Crystallogr., Sect. A: Found. Adv.* **2005**, *61*, 93−111.

(11) Mitchell, R. H. *Perovskites: Modern and Ancient*; Almaz Press Thunder Bay, 2002; Vol. *7*.

(12) King, G.; Woodward, P. M. Cation ordering in perovskites. *J. Mater. Chem.* **2010**, *20*, 5785−5796.

(13) Zhao, Q.; Liu, M.; Dai, J.; Deng, H.; Yin, Y.; Zhou, L.; Yang, J.; Hu, Z.; Agrestini, S.; Chen, K.; Pellegrin, E.; Valvidares, M.; Nataf, L.; Baudelet, F.; Tjeng, L. H.; Yang, Y.-f.; Jin, C.; Long, Y. High-pressure synthesis and ferrimagnetic ordering of the B-site-ordered cubic perovskite Pb_2FeOsO_6. *Inorg. Chem.* **2016**, *55*, 9816−9821.

(14) Martinez-Lope, M. J.; Alonso, J. A.; Casais, M. T. Synthesis, crystal and magnetic structure of the double perovskites A_2NiMoO_6 (A = Sr, Ba): A neutron diffraction study. *Eur. J. Inorg. Chem.* **2003**, *2003*, 2839−2844.

(15) Jin, C. Q. Using pressure effects to create new emergent materials by design. *MRS Adv.* **2017**, *2*, 2587−2596.

(16) Zhang, J.; Jia, Y.; Wang, X.; Li, Z.; Duan, L.; Li, W.; Zhao, J.; Cao, L.; Dai, G.; Deng, Z.; Zhang, S.; Feng, S.; Yu, R.; Liu, Q.; Hu, J.; Zhu, J.; Jin, C. A new quasi-one-dimensional compound Ba_3TiTe_5 and superconductivity induced by pressure. *NPG Asia Mater.* **2019**, *11*, 60.

(17) Li, M.-R.; Stephens, P. W.; Croft, M.; Deng, Z.; Li, W.; Jin, C.; Retuerto, M.; Hodges, J. P.; Frank, C. E.; Wu, M.; Walker, D.; Greenblatt, M. $Mn_2(Fe_{0.8}Mo_{0.2})MoO_6$: a double perovskite with multiple transition metal sublattice magnetic effects. *Chem. Mater.* **2018**, *30*, 4508−4514.

(18) Deng, Z.; Retuerto, M.; Liu, S.; Croft, M.; Stephens, P. W.; Calder, S.; Li, W.; Chen, B.; Jin, C.; Hu, Z.; Li, M.-R.; Lin, H.-J.; Chan, T.-S.; Chen, C.-T.; Kim, S. W.; Greenblatt, M. Dynamic ferrimagnetic order in a highly distorted double perovskite Y_2CoRuO_6. *Chem. Mater.* **2018**, *30*, 7047−7054.

(19) Deng, Z.; Kang, C. J.; Croft, M.; Li, W.; Shen, X.; Zhao, J.; Yu, R.; Jin, C.; Kotliar, G.; Liu, S.; Tyson, T. A.; Tappero, R.; Greenblatt, M. A pressure-induced inverse order-disorder transition in double perovskites. *Angew. Chem., Int. Ed. Engl.* **2020**, *59*, 8240−8246.

(20) Kobayashi, K.-I.; Kimura, T.; Sawada, H.; Terakura, K.; Tokura, Y. Room-temperature magnetoresistance in an oxide material with an ordered double-perovskite structure. *Nature* **1998**, *395*, 677−680.

(21) Azuma, M.; Takata, K.; Saito, T.; Ishiwata, S.; Shimakawa, Y.; Takano, M. Designed ferromagnetic, ferroelectric Bi_2NiMnO_6. *J. Am. Chem. Soc.* **2005**, *127*, 8889−8892.

(22) Knapp, M. C.; Woodward, P. M. A-site cation ordering in $AA'BB'O_6$ perovskites. *J. Solid State Chem.* **2006**, *179*, 1076−1085.

(23) Krockenberger, Y.; Mogare, K.; Reehuis, M.; Tovar, M.; Jansen, M.; Vaitheeswaran, G.; Kanchana, V.; Bultmark, F.; Delin, A.; Wilhelm, F.; Rogalev, A.; Winkler, A.; Alff, L. Sr_2CrOsO_6: end point of a spin-polarized metal-insulator transition by 5d band filling. *Phys. Rev. B: Condens. Matter Mater. Phys.* **2007**, *75*, 020404.

(24) Goto, M.; de Irujo-Labalde, X. M.; Saito, T.; García-Martín, S.; Shimakawa, Y. Successive and site-selective oxygen release from B-site-layer-ordered double perovskite Ca_2FeMnO_6 with unusually high valence Fe^{4+}. *Inorg. Chem.* **2020**, *59*, 2024−2029.

(25) Romero, F. D.; Patino, M. A.; Haruta, M.; Kurata, H.; Attfield, J. P.; Shimakawa, Y. Conversion of a defect pyrochlore into a double perovskite via high-pressure, high-temperature reduction of Te^{6+}. *Inorg. Chem.* **2020**, *59*, 343−349.

(26) Ye, X.; Zhao, J.; Das, H.; Sheptyakov, D.; Yang, J.; Sakai, Y.; Hojo, H.; Liu, Z.; Zhou, L.; Cao, L.; Nishikubo, T.; Wakazaki, S.; Dong, C.; Wang, X.; Hu, Z.; Lin, H.-J.; Chen, C.-T.; Sahle, C.; Efiminko, A.; Cao, H.; Calder, S.; Mibu, K.; Kenzelmann, M.; Tjeng, L. H.; Yu, R.; Azuma, M.; Jin, C.; Long, Y. Observation of novel charge ordering and spin reorientation in perovskite oxide $PbFeO_3$. *Nat. Commun.* **2021**, *12*, 1917.

(27) Azuma, M.; Sakai, Y.; Nishikubo, T.; Mizumaki, M.; Watanuki, T.; Mizokawa, T.; Oka, K.; Hojo, H.; Naka, M. Systematic charge distribution changes in Bi- and Pb-3d transition metal perovskites. *Dalton Trans.* **2018**, *47*, 1371−1377.

(28) Altomare, A.; Cuocci, C.; Giacovazzo, C.; Moliterni, A.; Rizzi, R.; Corriero, N.; Falcicchio, A. EXPO2013: a kit of tools for phasing crystal structures from powder data. *J. Appl. Crystallogr.* **2013**, *46*, 1231−1235.
(29) Toby, B. H. EXPGUI, a graphical user interface for GSAS. *J. Appl. Crystallogr.* **2001**, *34*, 210−213.
(30) Moretti Sala, M.; Martel, K.; Henriquet, C.; Al Zein, A.; Simonelli, L.; Sahle, C. J.; Gonzalez, H.; Lagier, M.-C.; Ponchut, C.; Huotari, S.; Verbeni, R.; Krisch, M.; Monaco, G. A high-energy-resolution resonant inelastic X-ray scattering spectrometer at ID20 of the European Synchrotron Radiation Facility. *J. Synchrotron Radiat.* **2018**, *25*, 580−591.
(31) Zhou, L.; Dai, J.; Chai, Y.; Zhang, H.; Dong, S.; Cao, H.; Calder, S.; Yin, Y.; Wang, X.; Shen, X.; Liu, Z.; Saito, T.; Shimakawa, Y.; Hojo, H.; Ikuhara, Y.; Azuma, M.; Hu, Z.; Sun, Y.; Jin, C.; Long, Y. Realization of large electric polarization and strong magnetoelectric coupling in $BiMn_3Cr_4O_{12}$. *Adv. Mater.* **2017**, *29*, 1703435.
(32) Isupov, V. A. Ferroelectric and antiferroelectric perovskites $PbB'_{0.5}B''_{0.5}O_3$. *Ferroelectrics* **2003**, *289*, 131−195.
(33) Howard, C. J.; Kennedy, B. J.; Woodward, P. M. Ordered double perovskites-a group-theoretical analysis. *Acta Crystallogr., Sect. B: Struct. Sci.* **2003**, *59*, 463−471.
(34) Vasala, S.; Karppinen, M. $A_2B'B''O_6$ perovskites: A review. *Prog. Solid State Chem.* **2015**, *43*, 1−36.
(35) Shannon, R. D.; Prewitt, C. T. Revised values of effective ionic radii. *Acta Crystallogr., Sect. B: Struct. Sci.* **1970**, *26*, 1046−1048.
(36) Fukuda, M.; Yamada, I.; Murata, H.; Hojo, H.; Hernandez, O. J.; Ritter, C.; Tanaka, K.; Fujita, K. Perovskite-type $CuNbO_3$ exhibiting unusual noncollinear ferrielectric to collinear ferroelectric dipole order transition. *Chem. Mater.* **2020**, *32*, 5016−5027.
(37) West, D. V.; Davies, P. K. Triclinic and monoclinic structures of $SrLaCuNbO_6$ and $SrLaCuTaO_6$ double perovskites. *J. Appl. Crystallogr.* **2011**, *44*, 595−602.
(38) Brown, I. D.; Altermatt, D. Bond-valence parameters obtained from a systematic analysis of the inorganic crystal-structure database. *Acta Crystallogr., Sect. B: Struct. Sci.* **1985**, *41*, 244−247.
(39) Guo, H.; Li, Z. W.; Zhao, L.; Hu, Z.; Chang, C. F.; Kuo, C.-Y.; Schmidt, W.; Piovano, A.; Pi, T. W.; Sobolev, O.; Khomskii, D. I.; Tjeng, L. H.; Komarek, A. C. Antiferromagnetic correlations in the metallic strongly correlated transition metal oxide $LaNiO_3$. *Nat. Commun.* **2018**, *9*, 43.
(40) Haverkort, M. W.; Csiszar, S. I.; Hu, Z.; Altieri, S.; Tanaka, A.; Hsieh, H. H.; Lin, H. J.; Chen, C. T.; Hibma, T.; Tjeng, L. H. Magnetic versus crystal-field linear dichroism in NiO thin films. *Phys. Rev. B: Condens. Matter Mater. Phys.* **2004**, *69*, 020408.
(41) Burnus, T.; Hu, Z.; Wu, H.; Cezar, J. C.; Niitaka, S.; Takagi, H.; Chang, C. F.; Brookes, N. B.; Lin, H.-J.; Jang, L. Y.; Tanaka, A.; Liang, K. S.; Chen, C. T.; Tjeng, L. H. X-ray absorption and x-ray magnetic dichroism study on Ca_3CoRhO_6 and Ca_3FeRhO_6. *Phys. Rev. B: Condens. Matter Mater. Phys.* **2008**, *77*, 205111.
(42) Chen, J.-M.; Chin, Y.-Y.; Valldor, M.; Hu, Z.; Lee, J.-M.; Haw, S.-C.; Hiraoka, N.; Ishii, H.; Pao, C.-W.; Tsuei, K.-D.; Lee, J.-F.; Lin, H.-J.; Jang, L.-Y.; Tanaka, A.; Chen, C.-T.; Tjeng, L. H. A complete high-to-low spin state transition of trivalent cobalt ion in octahedral symmetry in $SrCo_{0.5}Ru_{0.5}O_{3-\delta}$. *J. Am. Chem. Soc.* **2014**, *136*, 1514−1519.
(43) Nemrava, S.; Link, L.; Hu, Z.; Blaschkowski, B.; Liao, S.-C.; Lin, H.-J.; Chen, C.-T.; Chan, T.-S.; Tjeng, L. H.; Niewa, R. Synthesis and characterization of $BaLiRu_5O_{11}$, $BaCu_{1+x}Ru_{5-x}O_{11}$, and $BaLi_{1-x}Cu_{x+\delta}Ru_{5-\delta}O_{11}$: crystal structures and valence states. *Z. Anorg. Allg. Chem.* **2018**, *644*, 1691−1696.
(44) Agrestini, S.; Kuo, C.-Y.; Chen, K.; Utsumi, Y.; Mikhailova, D.; Rogalev, A.; Wilhelm, F.; Förster, T.; Matsumoto, A.; Takayama, T.; Takagi, H.; Haverkort, M. W.; Hu, Z.; Tjeng, L. H. Probing the J_{eff}=0 ground state and the Van Vleck paramagnetism of the Ir^{5+} ions in layered $Sr_2Co_{0.5}Ir_{0.5}O_4$. *Phys. Rev. B: Condens. Matter Mater. Phys.* **2018**, *97*, 214436.
(45) de Vries, M. A.; Mclaughlin, A. C.; Bos, J.-W. G. Valence bond glass on an fcc lattice in the double perovskite Ba_2YMoO_6. *Phys. Rev. Lett.* **2010**, *104*, 177202.
(46) Chen, K.; Mijiti, Y.; Agrestini, S.; Liao, S.-C.; Li, X.; Zhou, J.; Di Cicco, A.; Baudelet, F.; Tjeng, L. H.; Hu, Z. Valence state of Pb in transition metal perovskites $PbTMO_3$ (TM= Ti, Ni) determined from X-ray absorption near-edge spectroscopy. *Phys. Status Solidi B* **2018**, *255*, 1800014.
(47) Liu, Z.; Sakai, Y.; Yang, J.; Li, W.; Liu, Y.; Ye, X.; Qin, S.; Chen, J.; Agrestini, S.; Chen, K.; Liao, S.-C.; Haw, S.-C.; Baudelet, F.; Ishii, H.; Nishikubo, T.; Ishizaki, H.; Yamamoto, T.; Pan, Z.; Fukuda, M.; Ohashi, K.; Matsuno, K.; Machida, A.; Watanuki, T.; Kawaguchi, S. I.; Arevalo-Lopez, A. M.; Jin, C.; Hu, Z.; Attfield, J. P.; Azuma, M.; Long, Y. Sequential spin state transition and intermetallic charge transfer in $PbCoO_3$. *J. Am. Chem. Soc.* **2020**, *142*, 5731−5741.
(48) Zhao, J.; Gao, J.; Li, W.; Qian, Y.; Shen, X.; Wang, X.; Shen, X.; Hu, Z.; Dong, C.; Huang, Q.; Cao, L.; Li, Z.; Zhang, J.; Ren, C.; Duan, L.; Liu, Q.; Yu, R.; Ren, Y.; Weng, S.-C.; Lin, H.-J.; Chen, C.-T.; Tjeng, L.-H.; Long, Y.; Deng, Z.; Zhu, J.; Wang, X.; Weng, H.; Yu, R.; Greenblatt, M.; Jin, C. A combinatory ferroelectric compound bridging simple ABO_3 and A-site-ordered qudruple perovskite. *Nat. Commun.* **2021**, *12*, 747.
(49) Gagulin, V. V.; Korchagina, S. K.; Ivanova, V. V.; Shevchuk, Y. A. Synthesis and properties of Sr_2CoMoO_6 and Sr_2NiMoO_6. *Inorg. Mater.* **2003**, *39*, 625−626.
(50) Sakai, Y.; Yang, J.; Yu, R.; Hojo, H.; Yamada, I.; Miao, P.; Lee, S.; Torii, S.; Kamiyama, T.; Ležaić, M.; Bihlmayer, G.; Mizumaki, M.; Komiyama, J.; Mizokawa, T.; Yamamoto, H.; Nishikubo, T.; Hattori, Y.; Oka, K.; Yin, Y.; Dai, J.; Li, W.; Ueda, S.; Aimi, A.; Mori, D.; Inaguma, Y.; Hu, Z.; Uozumi, T.; Jin, C.; Long, Y.; Azuma, M. A-Site and B-Site charge orderings in an s-d level controlled perovskite oxide $PbCoO_3$. *J. Am. Chem. Soc.* **2017**, *139*, 4574−4581.
(51) Ramirez, A. P. Strongly geometrically frustrated magnets. *Annu. Rev. Mater. Sci.* **1994**, *24*, 453−480.
(52) Feng, H. L.; Arai, M.; Matsushita, Y.; Tsujimoto, Y.; Guo, Y.; Sathish, C. I.; Wang, X.; Yuan, Y.-H.; Tanaka, M.; Yamaura, K. High-temperature ferrimagnetism driven by lattice distortion in double perovskite Ca_2FeOsO_6. *J. Am. Chem. Soc.* **2014**, *136*, 3326−3329.
(53) Yan, J.-Q.; Zhou, J.-S.; Cheng, J. G.; Goodenough, J. B.; Ren, Y.; Llobet, A.; McQueeney, R. J. Spin and orbital ordering in $Y_{1-x}La_xVO_3$. *Phys. Rev. B: Condens. Matter Mater. Phys.* **2011**, *84*, 214405.
(54) Kumar, R.; Tomy, C. V.; Nagarajan, R.; Paulose, P. L.; Malik, S. K. Magnetization and heat capacity studies of double perovskite compounds Ba_2SmRuO_6 and Ba_2DyRuO_6. *Physica B* **2009**, *404*, 2369−2373.
(55) Eriksson, A. K.; Eriksson, S.-G.; Ivanov, S. A.; Knee, C. S.; Eriksen, J.; Rundlöf, H.; Tseggai, M. High temperature phase transition of the magnetoelectric double perovskite Sr_2NiMoO_6 by neutron diffraction. *Mater. Res. Bull.* **2006**, *41*, 144−157.

https://doi.org/10.1021/acs.chemmater.1c02826
Chem. Mater. 2022, 34, 97−106